Thermal Science and Engineering Progress xxx (xxxx) 104744

Contents lists available at ScienceDirect

Thermal Science and Engineering Progress

journal homepage: www.sciencedirect.com/journal/thermal-science-and-engineering-progress

Journal Cover Image

Residual properties and microstructural evolution of heated 3D printed concrete after exposure to water

Hongru Zhou [a, b, d], Linsen Zhang [a, d], Hideki Yoshioka [b, d], Muying Ge [a, d], Kai Wang [a, d], Bochao Sun [c, d], Ziyi Lu [a, d], Biao Zhou [a, b, *]

[a] Inner Mongolia Research Institute, China University of Mining and Technology (Beijing), Ordos 017010, China
[b] School of Emergency Management and Safety Engineering, China University of Mining and Technology (Beijing), Beijing 100083, China
[c] Department of Architecture, Faculty of Engineering, The University of Tokyo, Tokyo 113-8654, Japan
[d] College of Civil Engineering and Architecture, Zhejiang University, Hangzhou 310058, China

ARTICLE INFO

Keywords:
Fire protection
Fire resistance
High temperature
3D printed concrete

ABSTRACT

The progressive adoption of 3D printed concrete (3DPC) in construction necessitates a comprehensive evaluation of its performance under extreme thermal conditions, especially concerning post-fire residual safety. While previous research has largely focused on material behavior under slow cooling, the effect of rapid water cooling—representative of realistic firefighting operations—on the interlaminar zones of 3DPC remain poorly characterized. This work systematically examines the deterioration of 3DPC after exposure to temperatures reaching 800 °C followed by water quenching. Integrated experimental techniques, including mechanical testing, scanning electron microscopy, X-ray diffraction, thermogravimetry, and nitrogen adsorption analysis, reveal severe coupled damage mechanisms under the combined effect of high temperature and thermal shock. Key observations include a drastic reduction in compressive strength, exceeding 50% after 800 °C treatment, the addition of fibers has made the occurrence of cracks more complicated, and decomposition of hydration products accompanied by CaO rehydration leading to expansive fracture. A critical degradation threshold was identified between 400 °C and 600 °C, where concurrent physicochemical processes result in irreversible loss of integrity. The findings emphasize the vulnerability of printed interfaces to thermal shock and provide a foundational basis for designing damage-resistant 3DPC mixtures and improving fire safety standards in digital fabrication.

1. Introduction

The impact of various factors on building materials under fire exposure has been extensively studied in the field of fire safety and building engineering [1]. Previous research has made significant studies in understanding the deterioration of traditional building materials, such as reinforced concrete and steel structures, under high-temperature conditions, and the subsequent failure of structures [2]. These findings are of the utmost importance for the evaluation of a building's fire safety and recovery capabilities. In recent years, the building industry has witnessed a gradual adoption of 3D printing technology. As a novel building material, 3D printed concrete (3DPC) has garnered increasing attention due to its advantageous design characteristics and low cost [3,4]. However, there remains a critical gap in knowledge regarding the behavior of 3DPC in fire exposure, particularly under extreme conditions such as high temperature and rapid cooling.

High-temperature exposure is believed to be a major cause of the structural integrity failure of concrete [5–7]. Considering the building fire happens frequently in the world, many researchers have focused on the thermal performance of concrete [8]. It has been demonstrated that traditional concrete is susceptible to fissure expansion, strength loss, and microstructural degradation when exposed to elevated temperatures, particularly during the water-cooling phase [9]. In the aftermath of elevated temperatures, the implementation of a cooling process has been observed to exacerbate the expansion of internal fissures in concrete, thereby significantly reducing its strength [10]. Similar studies have indicated that the cooling rate of concrete specimens has a direct impact on the formation of fissures and the subsequent deterioration of strength [11]. However, the layered structure of 3DPC and its relatively weak interlayer cohesion contribute to a more complex deterioration process following exposure to fire [12]. Consequently, there is a paucity of research on the degradation mechanisms of 3DPC in the context of fire, particularly with regard to the impact on interlayer strength and

* zhoubiao1088@cumtb.edu.cn

https://doi.org/10.1016/j.tsep.2026.104744
Received 3 November 2025; Received in revised form 7 April 2026; Accepted 13 May 2026

microstructure following exposure to high temperatures and rapid cooling [13]. As 3D printing technology continues to advance, it becomes imperative to understand its performance under extreme conditions to ensure the structural integrity of constructed objects [14].

Existing research on the post-fire performance of concrete has mainly focused on traditional and ultra-high-performance concrete. Wouter et al. [15] studied the influence of different water cooling rates on traditional concrete after fire, indicating that rapid water cooling led to higher crack density and strength loss. However, there remains a critical gap in knowledge regarding rapid water cooling on 3DPC, especially in terms of crack generation, pore changes, and material strength attenuation after high-temperature exposure. Most of the existing research has focused on the material performance testing at room temperature and the physical and chemical changes after high-temperature exposure, but it lacks a comprehensive analysis of the microstructure changes of 3DPC after the combination of rapid water cooling and high-temperature exposure [8]. Napolitano et al. [16]mentioned that the layered structure of 3DPC might exhibit more significant performance degradation after fire exposure, especially the interlayer part might be severely affected by water cooling. Although the former research provides a fundamental understanding and highlights the unique interlayer damage of 3DPC after heating, few research have systematically studied the combined impact of high temperature and subsequent rapid water cooling on its structural integrity and microstructure evolution [1].

Differing from previously available work, the current work focuses on the degradation of 3DPC after rapid water cooling when exposed to high temperatures. In this contribution, through a series of macroscopic and microscopic experiments on 3DPC samples cooled by room-temperature water, the mechanical property loss and microstructure changes of 3DPC after high-temperature water cooling were discussed in detail. The correlation between strength loss and internal changes of 3DPC under different temperature treatments was introduced in detail. The influence of temperature and water-cooling treatment on 3DPC was clarified. The dynamic mechanism of high temperature and cooling treatment on the structure and pores of 3DPC was described.

2. Materials and experimental program

2.1. Raw materials

The 3DPC of this study comprises of Portland cement, river sand, water, basalt fiber (BF), polypropylene (PP) fiber and a variety of chemical additives. The mix proportion (by weight) of the raw materials used for mixture preparation is presented in Table.1. The specifications of basalt fibers are listed in Table. 2.

The cement was P.O. 42.5 Ordinary Portland Cement, sourced from Guangli Intelligent Technology Co., Ltd. The chemical composition, as determined by X-ray fluorescence (XRF) analysis, is as follows: SiO_2 45.545%, CaO 29.323%, Al_2O_3 11.327%, SO_3 3.352%, Fe_2O_3 2.918%, MgO 2.641%, K_2O 2.11127%, Na_2O 1.781%.

To enhance the fluidity and prolong the hardening time of cement, the powder-form superplasticizer (SP) and set retarder were added into raw materials. The inclusion of PP fiber and basalt fiber improved both the printability and workability, meanwhile the excellent properties of basalt fibers such as high strength, electrical insulation, corrosion resistance and high-temperature resistance, improved the performance of 3PDC.

Table 1
Mix proportion of raw materials used for 3D printable mixture (unit: kg/m^3).

Cement	Sand	Water	PP fiber	Basalt fiber	Super plasticizer	Set retarder
1000	1090	200	1.5	2.5	2.0	1.9

Table 2
Specifications of the basalt fibers.

	Length (mm)	Diameter (mm)	Density (g/cm3)	Elastic modulus (GPa)	Tensile strength (MPa)
Basalt fibers	18	7–15	2.63–2.65	91–110	1800–2200

2.2. Test specimen fabrication

The 3DPC specimen was fabricated using a printer equipped with a 20 mm round nozzle, and the printing speed was set to 20 mm/s (Fig. 1). The width and height of the printed mortar strip were 20 mm and 15 mm, respectively. The nozzle standoff distance (i.e., the vertical distance from the nozzle outlet to the top surface of the previously deposited strip) was maintained at 10 mm during printing. The coordinate system was defined as follows: the X-axis is the nozzle movement direction; the Y-axis is perpendicular to the nozzle movement direction and parallel to the bottom surface; and the Z-axis is the vertical printing direction. During the printing process, the nozzle moved back and forth in an S-shaped pattern layer by layer, and the printing process ended after the 7th layer was completed. After printing, the specimens were placed in a curing chamber at 20 ± 2 ˚C and 95 ± 5% relative humidity for 28 days. After curing, the samples were cut into 70.7 × 70.7 × 70.7 mm cubes to evaluate the mechanical properties of the 3D-printed samples. And experimental process diagram is shown in Fig. 2.

2.3. Testing and characterization methods

2.3.1. Elevated temperature

The specimens were heat-treated using a muffle furnace to simulate various fire exposure environments. The temperature was increased from room temperature to the target temperature (200 ˚C, 400 ˚C, 600 ˚C, and 800 ˚C) at a heating rate of 15 ˚C/min. When the temperature reaches the target temperature, maintain it for another 2 h. After heating was completed, the specimens were fully immersed in 5 L room-temperature water for 30 min to simulate firefighting conditions.

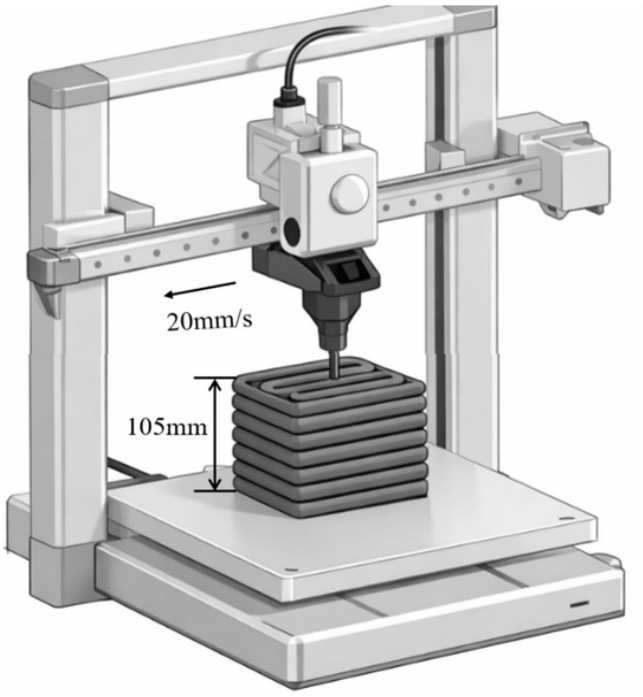

Fig. 1. 3D printing device.

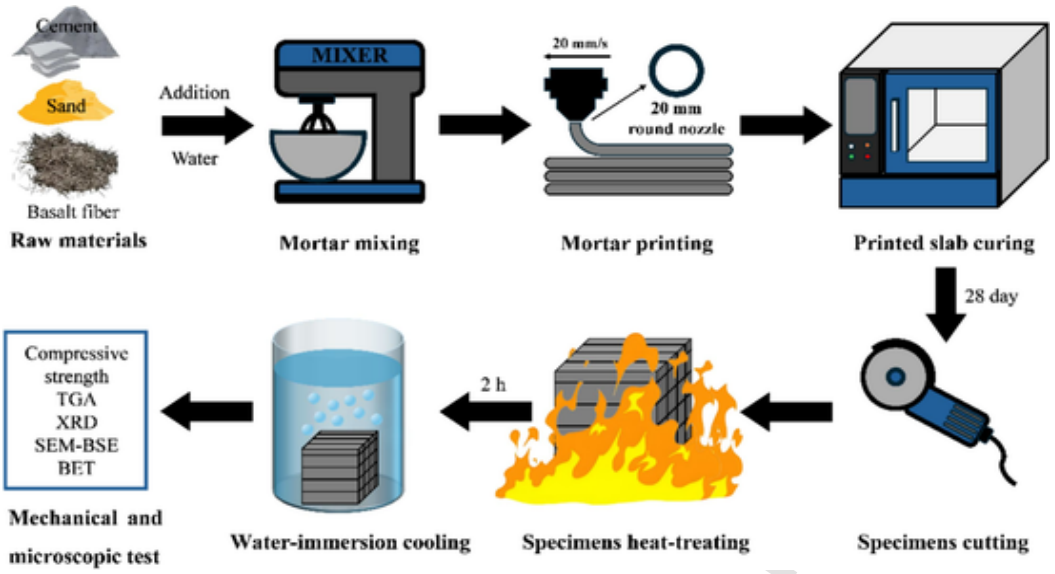

Fig. 2. Experimental process diagram.

During the immersion period, the cooling water was not refreshed, and no stirring or forced convection was applied; the system remained undisturbed throughout the entire process. The mass loss of the specimens before and after high-temperature exposure was recorded, and their mechanical properties were tested at room temperature.

2.3.2. Mechanical testing

Compressive strength tests were conducted using a computer-controlled testing machine (CMT6103) with a maximum load capacity of 200 tons. As shown in Fig. 3, the size of the experimental test block was 70.7 × 70.7 × 70.7 mm, and the pressing speed was set to 0.3 MPa/s. The compressive strength was tested along the Z directions, for each mechanical property, three specimens were tested, and the average value was reported to represent the mechanical characteristics.

2.3.3. Microscopic testing

Sampling locations for different microanalysis specimens are shown in Fig. 4. The samples for SEM were directly adhered to the conductive adhesive, and gold was sprayed for 45 s using the Quorum SC7620 sputtering coating instrument, with a gold spraying rate of 10 mA. Subsequently, the sample morphology was captured using a ZEISS GemiSEM 300 scanning electron microscope. During the morphology capture, the acceleration voltage was 3 kV, and the detector was a SE2 secondary electron detector. SEM provides high-resolution images, revealing the distribution and size of pores, cracks and other microstructure features.

2.3.4. X-ray diffraction and analysis

After heat treatment and 30 min water cooling, then extract a part of the sample, crush and grind this part into fine powder for XRD analysis. The conclusions of XRD tests can characterize the crystalline phases

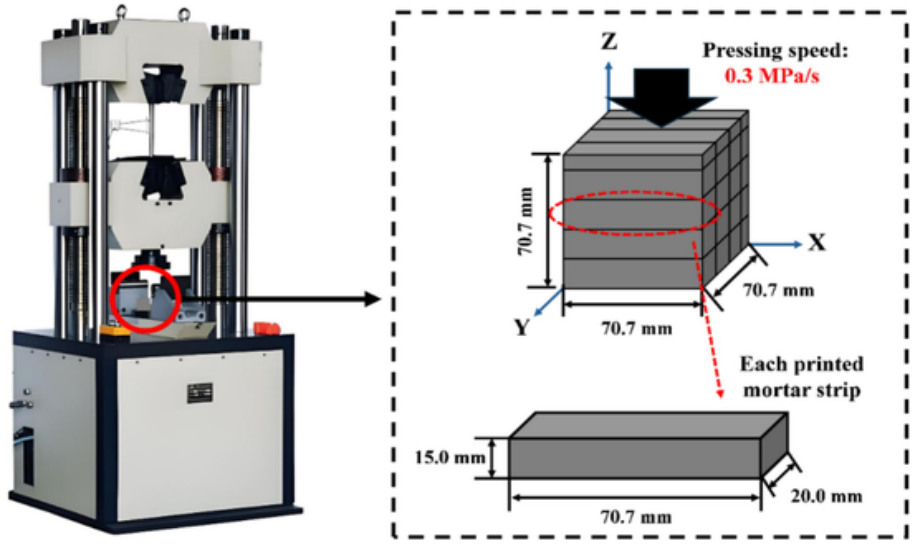

Fig. 3. Compressive strength test.

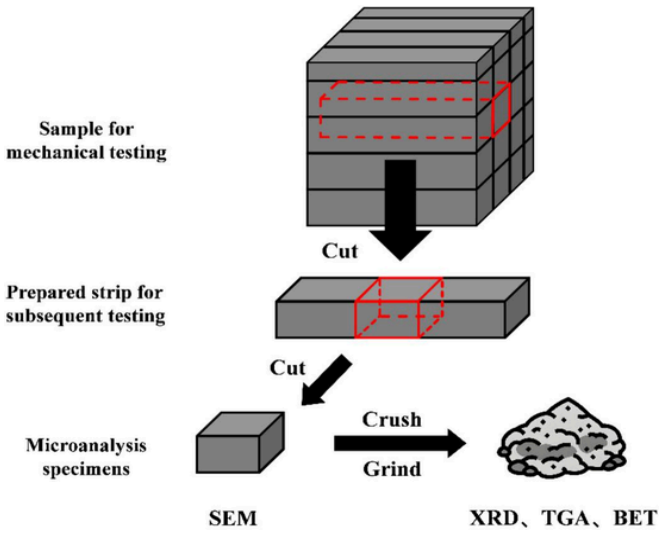

Fig. 4. Sampling location for microanalysis specimens.

present in 3DPC and demonstrate the differences of the crystalline phase under different temperature exposure conditions.

2.3.5. Thermogravimetric analysis

Extract fragments of the specimens and grind them into fine powders for thermogravimetric analysis (TGA). Then the powder samples were directly heated from room temperature to 900 °C at 10 °C/min in nitrogen atmosphere. This method continuously records the mass loss of sample powder during the uniform heating process, thereby generating a thermal spectrum with information about pyrolysis behavior. The thermal decomposition process of the sample is analyzed through the mass loss curve, and then the thermal stability of the sample components is obtained.

2.3.6. BET analysis

Nitrogen adsorption–desorption isotherms were measured using a specific surface area and porosity analyzer (Micromeritics APSP 2460). Prior to the analysis, the samples were crushed and sieved to obtain fine powders. Approximately 0.2–0.3 g of the powdered sample from each group was accurately weighed and placed in the analysis tube. To remove any moisture and contaminants adsorbed on the surface, the samples were degassed under vacuum at 120 °C for a minimum of 8 h. The analysis was performed using high-purity N_2 as the adsorbate at its boiling temperature (77 K). The adsorption–desorption isotherms were obtained by measuring the volume of N_2 adsorbed and desorbed by the sample at a series of relative pressures (P/P_0) ranging from 0 to 0.995.

3. Results and discussion

3.1. Mass loss rate

The mass loss of 3DPC specimens after high-temperature exposure and rapid water cooling was determined by measuring the weight change before and after thermal treatment. Prior to heating, all specimens were weighed using an electronic balance with an accuracy of ± 0.01 g to obtain the initial mass (M_0). After thermal exposure, the specimens were immediately subjected to rapid water cooling. And all specimens were oven-dried at 60 °C for 24 h until a constant mass was achieved and then weighed to obtain the residual mass (M_1). The mass loss rate was calculated using the following equation: Residual Mass Ratio (%) = $M_1/M_0 \times 100$. For each temperature condition, three parallel specimens were tested, and the average value was reported.

As shown in Fig. 5, the residual mass ratio of the specimens decreases progressively with the exposure temperature. The data indicates a noticeable decrease in residual mass when the specimens are exposed to rapid water cooling after high-temperature exposure, in addition to the effects of thermal heating alone.

At 20 °C, the residual mass ratio remained at 100%, indicating stable material behavior at ambient temperature. When the temperature increased to 200 °C, the residual mass ratio dropped to 96.4% (a mass loss of 3.6%), mainly attributed to the evaporation of free water and initial dehydration of C-S-H gel [17,18]. A similar trend was observed at 400 °C, with the residual mass ratio falling to 93.7% (a mass loss of 6.3%). This reduction is primarily due to the dihydroxylation of portlandite ($Ca(OH)_2$) and the further breakdown of C-S-H gel [19,20]. At 600 °C, the residual mass ratio decreased to 91.4% (an 8.6% mass loss), as both calcium carbonate ($CaCO_3$) decomposition and transformation of C-S-H into anhydrous silicates occurred [21]. However, the coupled condition of high-temperature exposure and rapid water-cooling resulted in a severe mass loss. The rapid cooling process creates differential thermal expansion, causing external layers to contract faster than the interior, which induces further cracking and mass loss.

At the highest temperature of 800 °C, the residual mass ratio reached its lowest point of 86.3% (a total mass loss of 13.7%), reflecting the complete breakdown of hydration products and the transformation of the material into a brittle, ceramic-like structure [20]. The combined effect of exposure to 800 °C and subsequent water cooling led to a massive loss in mass. This is due to the combination of thermal shock and subsequent microcracking, which dramatically increases the material's porosity and accelerates the degradation process [22].

Importantly, as illustrated by the error bars in Fig. 5, the standard deviations of the residual mass ratio remain remarkably low across all temperature groups. This low statistical variability demonstrates the excellent uniformity of the 3DPC specimens prepared in this study.

In summary, the results clearly show that the mass loss of 3DPC significantly increases with higher temperatures and the introduction of rapid cooling, especially above 400 °C. However, supported by the remarkably low statistical dispersion of the data, it is evident that this severe thermal degradation and rapid-cooling-induced damage propagate in a highly uniform rather than through stochastic, localized failure. Therefore, while the additional internal stresses and severe microcracking from rapid cooling must be stringently considered in 3DPC applications involving fire or thermal shock scenarios, the macro-level struc-

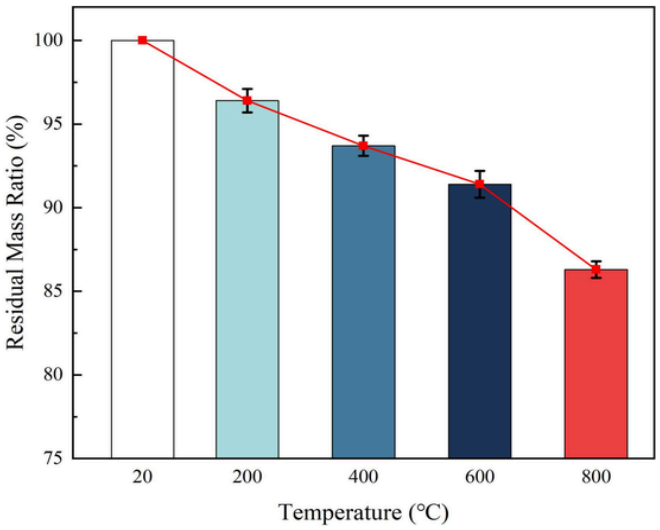

Fig. 5. Residual Mass Ratio of 3DPC at different temperatures.

tural deterioration behavior of this matrix remains exceptionally stable and predictable.

3.2. Compressive strength

The residual compressive strength of 3DPC after high-temperature exposure and rapid water cooling, a key indicator of post-fire load capacity, is shown in Fig. 6. Strength declines continuously with temperature: from a baseline of 38.03 MPa at 25 °C to 33.37 MPa (−12.3%) at 200 °C, 25.00 MPa (−34.3%) at 400 °C, 13.93 MPa (−63.4%) at 600 °C, and 4.87 MPa (−87.2%) at 800 °C. This monotonic reduction underscores the severe compounded damage from heating and thermal shock. At 200 °C, free water evaporation creates pore pressure; melting PP fibers (~165 °C) form micro-channels that relieve pressure but leave interconnected voids [23,24]. Near 400 °C, C–S–H dehydration and portlandite dehydroxylation further weaken the matrix [13]. Water quenching then induces severe thermal shock due to steep thermal gradients, generating tensile stresses that cause surface microcracking. These new cracks combine with pre-existing voids, increasing porosity and explaining the strength loss at 200 and 400 °C. Beyond 400 °C, damage intensifies through phase changes and thermal shock. The α–β quartz transition at 573 °C causes volumetric expansion, internal cracking, and ITZ debonding [22]. Basalt fibers temporarily bridge cracks and delay failure [25], but cannot counteract overall embrittlement.The thermal shock effect is much more severe at these temperatures. The rapid contraction of the outer surface violently propagates the internal microcracks already created by the quartz transformation, turning them into major, interconnected crack networks. The basalt fibers, while still present, cannot prevent the failure of the now extremely brittle matrix. By 600 °C, $Ca(OH)_2$ dehydroxylation completes, and $CaCO_3$ decarbonation occurs by 800 °C, both yielding reactive CaO [3,8]. Quenching at 800 °C allows water to infiltrate cracks and react with CaO, causing rehydration ($CaO + H_2O \rightarrow Ca(OH)_2$) with intense expansive pressure. This micro-explosive disintegration, combined with thermal shock, explains the near-total strength loss and failure of basalt fiber reinforcement due to matrix destruction [22,25].

As indicated by the narrower error bars in Fig. 6, the standard deviation of compressive strength noticeably decreases at extreme temperatures (600–800 °C with quenching). This reveals a fundamental shift in the failure mechanism. At lower temperatures, failure is driven by stochastically distributed manufacturing defects (the "weakest link" principle), resulting in high variability. However, extreme thermal shock induces saturated, pervasive microcracking. This transition from localized defect-driven fracture to uniform global matrix disintegration drops the residual strength to a consistently low baseline, inherently diminishing statistical dispersion.

3.3. XRD analysis

X-ray diffraction (XRD) was employed to characterize the phase composition of 3DPC specimens at different temperatures (RT, 200 °C, 400 °C, 600 °C, and 800 °C) [26], as shown in Fig. 7. At room temperature, the XRD pattern exhibits distinct diffraction peaks corresponding to portlandite [$Ca(OH)_2$], calcite ($CaCO_3$), quartz (SiO_2), and a crystalline calcium silicate hydrate phase [$Ca_3Si_2O_4(OH)_6$]. Quartz, derived from the sand or aggregate in the concrete, remains inert and structurally stable at low temperatures. Thus, the primary crystalline phases at ambient conditions consist of hydration products ($Ca(OH)_2$ and C–S–H), along with minor carbonate phases and inert quartz filler. Upon heating to 200 °C, only minor changes are observed in the XRD pattern compared with RT. Portlandite remains largely intact, as $Ca(OH)_2$ exhibits considerable thermal stability below approximately 200 °C and undergoes negligible decomposition. However, dehydration of the C–S–H phase has begun. Previous thermal analysis studies have shown that part of the bound water in C–S–H gel is released in the range of approximately 150–250 °C. Correspondingly, the diffraction peaks of hydrated calcium silicate show slight intensity reduction or peak broadening, indicating partial loss of structural water [27]. Nevertheless, most of the C–S–H crystalline structure remains present at this temperature. Calcite remains stable, and quartz remains unchanged. Overall, heating to 200 °C primarily induces initial dehydration of the C–S–H phase, while portlandite and other crystalline phases remain essentially unaffected. At 400 °C, significant phase transformations are evident in the XRD pattern. The diffraction peaks of portlandite decrease markedly in intensity, indicating substantial decomposition of $Ca(OH)_2$ at this stage. Indeed, $Ca(OH)_2$ dehydroxylates at approximately 400–450 °C, producing calcium oxide and water. The release of structural water generates additional porosity, whereas the resulting CaO is not clearly visible in the XRD pattern due to its low crystallinity or very fine particle size. Calcite remains stable at 400 °C, with its diffraction peaks essentially unchanged. Heating to 600 °C results in more pronounced changes in phase composition and diffraction patterns. At this stage, calcite begins to undergo notable decomposition (decarbonation). Consequently, by 600 °C, part of the original $CaCO_3$ has been transformed, leading to weakened calcite diffraction peaks. By this temperature, the original hydration products have almost completely de-

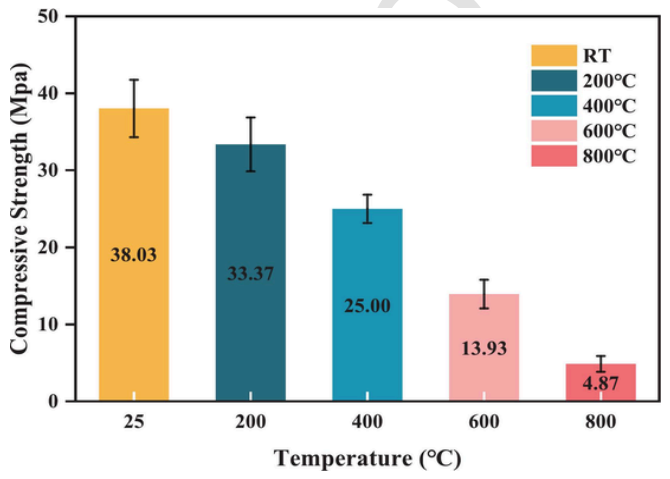

Fig. 6. Compressive strength of 3DPC at different temperatures (RT, 200 °C, 400 °C, 600 °C, 800 °C).

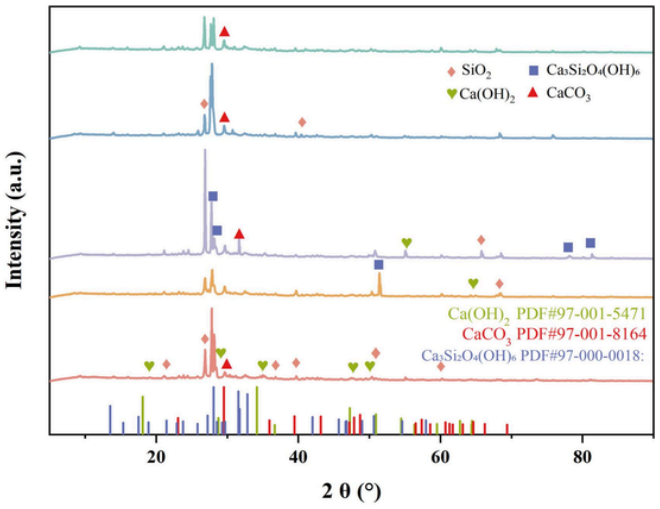

Fig. 7. XRD pattern of 3DPC at different temperature.

composed—portlandite has long since disappeared, and C–S–H gel (including afwillite) is fully dehydrated—greatly impairing the integrity of the microstructure. At 800 ˚C, any $Ca(OH)_2$ or C–S–H phases present at lower temperatures have completely disappeared, leaving only anhydrous products. The diffraction peaks of $CaCO_3$ are essentially absent [28]. Quartz remains detectable, retaining its crystalline structure.

3.4. TG analysis

To evaluate the influence of different pretreatment temperatures on the thermal stability of hydration products, Thermogravimetric analysis (TGA) tests were conducted on five groups of samples at room temperature (RT), 200 ˚C, 400 ˚C, 600 ˚C and 800 ˚C, as shown in Fig. 8. Based on the thermal decomposition characteristics of the cement-based system, the curve is divided into four representative temperature zones: 50–150 ˚C (free water and weakly bound water), 150–350 ˚C (C-S-H gel-structured water), 400–500 ˚C (calcium hydroxide $Ca(OH)_2$, abbreviated as CH, dehydroxylation), 650–800 ˚C ($CaCO_3$ decarbonization). The segmented weight loss and residual mass of each sample are shown in Table.3 [29,30].

For samples at room temperature, ΔW at 0–150 ˚C is 7.13%, showing significant free/weakly bound water. At 150–350 ˚C, the weight loss is 3.96%, corresponding to the continuous release of water in the C-S-H gel structure. At 400–500 ˚C, the CH window showed a weight loss of 0.72%, and the Differential Thermogravimetric (DTG) indicated the presence of a weak peak within the temperature range (slightly overlapping with the tail section of the C-S-H deep dehydration). The weight loss at 650–800 ˚C is 2.10%, which is caused by the decarburization of calcite [31]. These thermal events clearly demonstrate that the room-temperature cured sample contains abundant hydration products (e.g., C–S–H gel and $Ca(OH)_2$) as well as a certain amount of carbonation product ($CaCO_3$). The ample presence of hydration products imparts good macroscopic mechanical properties to the material, as the dense microstructure contributes to higher strength.

For the samples heated at 200 ˚C, the weight loss at 50–150 ˚C dropped to 4.49%, indicating that a considerable proportion of free/weakly bound water was driven away during the preheating stage. At 150–350 ˚C, the weight loss was 2.66%, and the detachable amount of C-S-H decreased, indicating that most of the surface adsorbed water and some interlayer water of the C-S-H gel had been removed during the heat treatment process. The CH window at 400–500 ˚C was 0.74%, approximately the same as RT (0.72%), and the difference was within the typical error range of Thermogravimetric (TG), with no significant change. The weight loss at 650–800 ˚C is 2.44%, similar to that of RT.

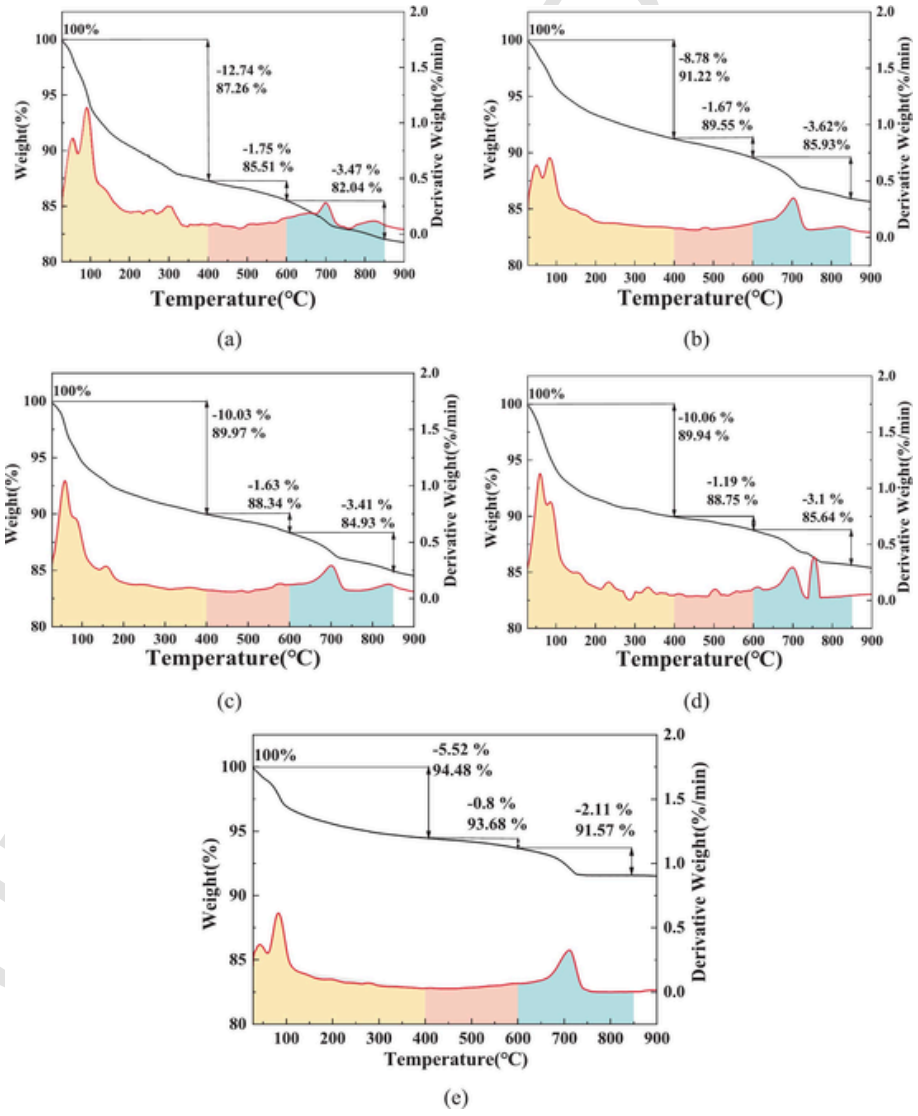

Fig. 8. Differential Thermogravimetric (DTG) and Thermogravimetric (TG) curves of 3DPC at different temperatures:(a) RT (b)200 ˚C (c) 400 ˚C (d)600 ˚C (e)800 ˚C.

Table 3
Weight Loss at each stage of 3DPC at different temperatures (20 °C, 400 °C, 600 °C, 800 °C).

	50–150 °C	150–350 °C	400–500 °C	650–800 °C
20 °C	7.13%	3.96%	0.72%	2.10%
200 °C	4.49%	2.66%	0.74%	2.44%
400 °C	5.79%	2.67%	0.66%	2.19%
600 °C	6.16%	2.25%	0.46%	2.41%
800 °C	3.09%	1.44%	0.30%	1.74%

The mass loss of carbonate decomposition is also similar to that of RT samples, which means that the treatment at 200 °C has no significant effect on the presence of $CaCO_3$ [31]. Overall, the sample after 200 °C treatment retains the key TG features of major hydrates (such as $Ca(OH)_2$), but its low-temperature dehydration peaks are diminished due to the partial water loss and structural rearrangement incurred at 200 °C. The resulting microstructure is slightly relaxed, which may cause a minor decline in mechanical strength compared to the RT sample.

For the sample heated at 400 °C, the weight loss at 50–150 °C was 5.79%, which was higher than 200 °C but still lower than RT. This indicates that the sample has a certain rehygroscopic capacity after the high-temperature water cooling process. The weight loss at 150–350 °C is 2.67%, which is comparable to that at 200 °C, indicating that the redetachable capacity of C-S-H continues to be limited. The CH window at 400–500 °C was 0.66%, further decreasing compared to RT/200 °C, but the decrease was relatively slow. In this study, under the path of "heating and holding → water cooling → drying → then TG/DTG", the CH dehydroxylation peak in the 400–500 °C range did not disappear but was significantly weakened due to the mechanical "forward shift + overlap + transfer". Specifically: (i) The secondary/low-crystallization CH induced by high-temperature treatment and water cooling begins to dehydroxyl at 300–380 °C, overlapping with the C-S-H dehydration tail section, which dilutes the conventional main peak around 450 °C. It has been reported in the literature [32] that the CH dehydroxylation event of the slurry treated at high temperature shifts to the low-temperature position, and the dehydroxylation peak of the "secondary CH" can shift from around 450 °C to approximately 410 °C. (ii) Carbonization during water cooling/exposure causes part of the CH mass loss to "move" from 400 to 500 °C to the $CaCO_3$ decarburization section at 650–800 °C, thereby further weakening the DTG peak in the regular window [33]. The weight loss is 2.19% at 650–800 °C, which is similar to that at 200 °C. These thermal analysis results indicate that at a high temperature of 400 °C, the primary gelation phase in the C-S-H gel is destroyed, with significant dehydration. $Ca(OH)_2$ begins to decompose, leading to an increase in microscopic porosity and a further decrease in macroscopic strength.

For the sample heated at 600 °C, the weight loss was 6.16% at 50–150 °C, slightly higher than that at 400 °C. High temperature combined with water cooling and thermal shock may increase the number of holes/crack channels and the specific surface area, leading to an increase in moisture absorption during subsequent storage. At 150–350 °C, the weight loss was 2.25%, which continued to decrease, indicating that the decomposable structural water of C-S-H further decreased. The CH window at 400–500 °C significantly decreased to 0.46%, indicating that after preheating at 600 °C, the remaining CH in the system that could be dehydroxylated at the conventional 400–500 °C was less (meanwhile, the low-crystalline CH dehydroxylation temperature of regeneration moved forward and overlapped with the II zone, reducing the net weight loss at the conventional window [34]). A weight loss of 2.41% at 650–800 °C indicates that calcium carbonate still exists. At a high temperature of 600 °C, the microstructure of the sample severely deteriorated, forming many pores and cracks. The cement matrix almost lost its bonding capacity, resulting in a sharp decline in macroscopic mechanical properties and a loss of about half of the original strength. However, in the moist environment after cooling, some hydration reactions and secondary cementation reactions of CaO (such as the formation of a small amount of new C-S-H) will occur [23].

For the samples heated at 800 °C, only 3.09% were obtained from 50 to 150 °C, which was the lowest in the entire group. At 150–350 °C, it is 1.44%. At 400–500 °C, the CH window is the lowest at 0.30%, and there is almost no peak in DTG, which is in line with the expectation that CH has decomposed in large amounts during the preheating stage with very little regeneration, and the dehydroxylation of low-crystallized CH has moved forward and the signal is dispersed. The weight loss at 650–800 °C is 1.74%, which is also the lowest, indicating that the content of decarbonizable $CaCO_3$ is the least (it has been consumed in advance during the high-temperature stage, and the re-carbonization is relatively restricted). At 800 °C, all the cementitious hydrates (such as C-S-H, $Ca(OH)_2$, etc.) have decomposed, and the cement matrix basically returns to a state similar to the original clinker minerals. Concrete loses most of its strength at temperatures above 800 °C. The macroscopic mechanical properties of the samples treated at 800 °C decreased sharply [34].

It is noteworthy that the dehydration peak within 0–150 °C, which would normally diminish after high-temperature exposure, remains observable in all specimens due to water reabsorption during the water-cooling process. However, with increasing pretreatment temperature, the dehydration peaks associated with more strongly bound water at higher temperatures progressively weaken and eventually disappear. Consequently, only the low-temperature peak corresponding to physically stored free water introduced during water cooling remains prominent.

Meanwhile, the dehydroxylation peak of $Ca(OH)_2$ (CH), typically expected at 430–470 °C, appears consistently weak or indistinct in all samples, particularly in those pretreated above 400 °C. This phenomenon can be attributed to the coupled effects of phase consumption, peak superposition, crystallinity alteration, and redistribution of mass loss across different temperature intervals.

First, partial carbonation occurring during cooling and subsequent exposure converts a portion of CH into $CaCO_3$, effectively transferring part of the theoretical mass loss from the 400–500 °C interval to the 650–800 °C decarbonation region. As a result, the net detectable CH-related mass loss within its conventional temperature window is reduced.

Second, when the pretreatment temperature reaches or exceeds 400 °C, CH undergoes partial dehydroxylation during the heating stage itself, significantly decreasing the residual CH content available for subsequent TG analysis. For specimens treated at 600 °C, and particularly at 800 °C, most primary CH has already decomposed prior to testing, leaving only trace amounts capable of producing a discernible DTG signal.

Third, high-temperature damage combined with water cooling may promote the rehydration of CaO, leading to the formation of secondary or poorly crystalline CH. Such low-crystallinity CH exhibits reduced thermal stability, and its dehydroxylation may shift forward to approximately 300–380 °C, overlapping with the tail region of C–S–H dehydration. This "forward shift and overlap" effect weakens the conventional main CH peak near 450 °C, resulting in a broadened and attenuated DTG signal rather than a sharp characteristic maximum.

Finally, progressive microstructural deterioration at elevated temperatures increases porosity and structural heterogeneity, causing thermal decomposition events to become more dispersed and thereby smoothing DTG features. Therefore, the absence of a pronounced CH peak does not necessarily indicate the complete disappearance of CH; rather, it reflects the combined influence of prior thermal decomposition, carbonation-induced mass redistribution, reduced crystallinity, and overlapping dehydration processes.

As shown in Fig. 7(e), The persistence of a distinct $CaCO_3$ decomposition peak after 800 °C pretreatment does not necessarily indicate in-

complete decomposition during the heating stage; rather, it is more plausibly attributed to post-thermal recarbonation. Although thermodynamically $CaCO_3$ approaches complete decomposition into CaO and CO_2 at approximately 750–800 ˚C, the CaO formed at high temperature exhibits high chemical reactivity. During subsequent water cooling and air exposure, CaO may first undergo rehydration to form CH, which can then rapidly react with atmospheric CO_2 to regenerate $CaCO_3$. Therefore, the $CaCO_3$ decarbonation peak detected during TG analysis of the specimen treated at 800 ˚C largely represents newly formed carbonate generated during the cooling and storage stages, rather than residual original $CaCO_3$ that failed to decompose at high temperature.

3.5. BET analysis

Specific surface area (BET) analysis is an important method for evaluating the microscopic pore structure of materials and is widely used in studying the adsorption performance, porosity and their relationship with performance of materials [35,36]. High-temperature treatment has a significant impact on the microstructure of cement-based materials, thereby affecting their specific surface area and pore volume. This section conducts BET analysis on 3DPC samples treated at different temperatures (room temperature, 200 ˚C, 400 ˚C, 600 ˚C, and 800 ˚C) to explore the influence of high temperature on their specific surface area and pore volume, as shown in Fig. 9. The adsorption–desorption isotherms were interpreted according to the International Union of Pure and Applied Chemistry (IUPAC) classification system for physisorption isotherms, which categorizes isotherms into Types I–VI based on pore structure characteristics. The quantitative values of specific surface area and total pore volume obtained from BET analysis are summarized in Table. 4, which provide direct evidence for the temperature-induced pore structure evolution.

As shown in Table 4, the specific surface area at room temperature is 7.16 m^2/g and the total pore volume is 0.028 cm^3/g, which serve as the baseline for evaluating subsequent thermal damage. At this point, the microstructure of the sample is relatively dense, mainly composed of calcium silicate hydrate (C-S-H) gel and calcium hydroxide hydrate ($Ca(OH)_2$) [18]. The isotherms of the samples at room temperature exhibit characteristics of a combination of Type I and Type IV isotherms according to the IUPAC classification. Type I isotherms are typically associated with microporous materials, while Type IV isotherms are characteristic of mesoporous materials and are usually accompanied by hysteresis loops due to capillary condensation. In the low P/P0 range, the adsorption capacity increases rapidly, indicating that the sample contains many micropores and small mesopores. With the increase of P/P0, the adsorption capacity gradually stabilizes, indicating pore saturation. This dense microstructure endows the material with high mechanical strength and low porosity at room temperature, demonstrating excellent stability and structural integrity.

The isotherms of the samples pretreated at 200 ˚C exhibit the characteristics of type IV hysteresis loops, similar to those of samples at room temperature, but with relatively lower adsorption capacity. Although the hysteresis loop still exists, its width is smaller than that of the samples at room temperature, indicating a reduction in the volume of the microporous part. However, mesopores still dominate. Although the hysteresis loop persists after treatment at 200 ˚C, its reduced width compared with the room-temperature sample indicates a decrease in micropore volume, while mesopores remain dominant. However, mesopores still dominate. Specifically, the specific surface area decreased to 6.05 m^2/g after treatment at 200 ˚C, and the total pore volume was 0.028 cm^3/g. The increase in temperature led to the release of some moisture, especially the adsorption of moisture and the removal of some crystalline water in the C-S-H gel, which caused an initial change in the pore structure of the sample. Despite this, the changes in porosity and specific surface area at 200 ˚C were relatively small. Therefore, at this temperature, the decrease in specific surface area is not significant, the microstructure of the material remains relatively intact, and its mechanical properties have not been greatly affected. The decrease in specific surface area from 7.16 m^2/g to 6.05 m^2/g corresponds to an approximate reduction of 15%, while the total pore volume remains nearly unchanged, indicating that dehydration mainly affects micropores without significantly altering overall pore connectivity.

When the temperature rises to 400 ˚C, the specific surface area of 3DPC further decreases to 5.29 m^2/g, and the total pore volume drops to 0.026 cm^3/g. This change mainly stems from the further dehydration and decomposition of hydration products. At this stage, the isotherms show a more obvious type IV hysteresis loop, and the adsorption capacity is further reduced compared with the samples at room temperature and 200 ˚C. After high-temperature treatment, the microporous structure of the sample was further damaged, and the ratio of mesopores to macropores increased, indicating that the pore structure contracted. The hysteresis loop becomes more pronounced, especially in the range where P/P0 > 0.3, indicating an increase in the proportion of macropores, which is consistent with the pore reconstruction process after high-temperature treatment. Within this temperature range, $Ca(OH)_2$ begins to dehydrate and convert into CaO, while the hydrated water content of C-S-H gel gradually decreases, leading to further changes in the pore structure. Scanning electron microscope images show that the samples at 400 ˚C exhibit fine cracks and pore expansion, and the dissolution of some hydration products leads to an increase in porosity [22]. Although the porosity slightly increased, compared with the changes under high-temperature conditions, the pores of the samples treated at 400 ˚C still maintained a smaller scale and uniform distribution. At 400 ˚C, the specific surface area further decreases to 5.29 m^2/g, representing an overall reduction of approximately 26% compared with room temperature, while the total pore volume declines to 0.026 cm^3/g. This confirms that progressive dehydration and partial decomposition of hydration products lead to pore coarsening and structural contraction.

At a high temperature of 600 ˚C, the changes in specific surface area and pore volume become more significant. At this point, the specific surface area increased to 5.64 m^2/g, and the total pore volume dropped to 0.023 cm^3/g. The isotherm changes more significantly, and the hysteresis loop further increases, especially in the higher P/P0 range, showing a larger pore volume. The adsorption capacity further declined, especially with a significant reduction in micropore adsorption within the low P/P0 range, indicating that the pore structure within the material has undergone severe collapse or reconstruction. The treatment at 600 ˚C led to almost complete dehydration of C-S-H and $Ca(OH)_2$, and the decomposition of hydration products caused severe degradation of the microstructure of the material. With the gradual decomposition of C-S-H and $Ca(OH)_2$, the overall strength of the material drops significantly and the pore structure tends to be loose. At 600 ˚C, although the total pore volume reaches its minimum value (0.023 cm^3/g), the specific surface area slightly increases to 5.64 m^2/g. The divergence between these two parameters suggests the initiation of microcracks, which increase internal surface area while the overall pore volume remains limited.

The most significant change occurred at 800 ˚C, where the specific surface area jumped to 6.89 m^2/g and the total pore volume was 0.043 cm^3/g, demonstrating a much higher specific surface area and pore volume than samples treated at other temperatures. The isotherms of the samples pretreated at 800 ˚C show type IV hysteresis loops, which are almost entirely microporous regions, while micropores and mesopores are almost completely lost. The appearance of the hysteresis loop indicates that the material still has a certain capillary coagulation effect [37], but the overall porosity has been significantly reduced, especially the disappearance of small pores. The occurrence of this phenomenon is closely related to high-temperature pyrolysis at 800 ˚C. At 800 ˚C, C-S-H and $Ca(OH)_2$ almost completely decompose, and the microstructure in the sample is damaged, forming a large number of microcracks and

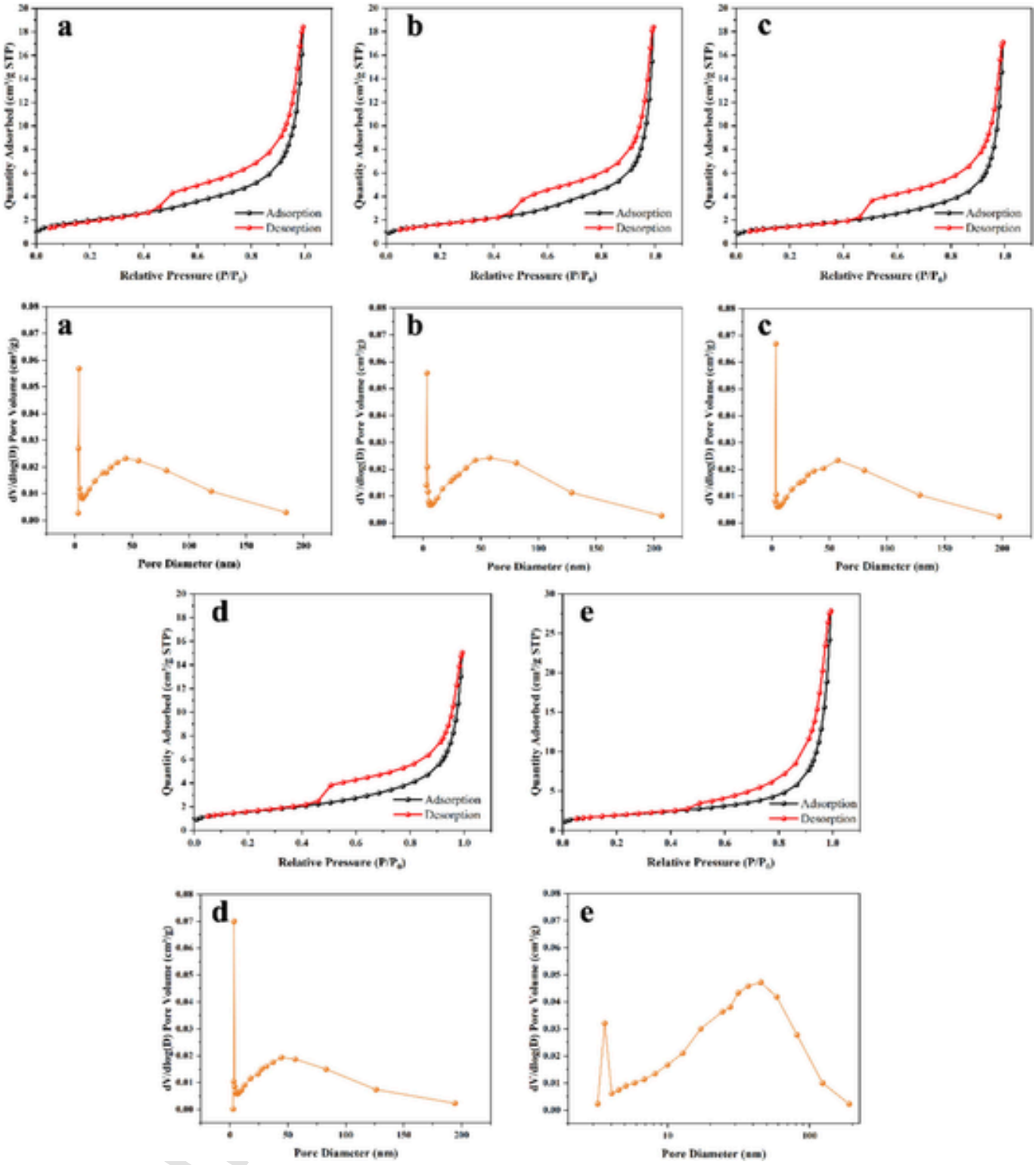

Fig. 9. Specific surface area and pore characteristics of 3DPC after high-temperature and water cooling:(a) RT (b) 200 °C (c) 400 °C (d)600 °C (e) 800 °C. The adsorbed gas volume is expressed at standard temperature and pressure (STP, 273.15 K and 1 atm).

pores. Meanwhile, some mineral phases, such as calcium silicate (CaO) and calcite ($CaCO_3$), underwent crystal phase changes, leading to the formation of new pore networks and larger pore diameters. Scanning electron microscope images also show that the microstructure of the 800 °C sample is almost completely cracked, presenting a distinct brittle structure and large-scale pore expansion [38]. This high-temperature treatment causes the material's strength to almost be lost. At 800 °C, the specific surface area increases to 6.89 m^2/g, and the total pore volume rises sharply to 0.043 cm^3/g, corresponding to increases of approximately 22% and 85% relative to room temperature, respec-

Table 4
BET specific surface area and total pore volume of samples treated at different temperatures (20 °C, 400 °C, 600 °C, 800 °C).

Treatment temperature (°C)	BET specific surface area (m^2/g)	Total pore volume (cm^3/g)
RT	7.16	0.028
200 °C	6.05	0.028
400 °C	5.29	0.026
600 °C	5.64	0.023
800 °C	6.89	0.043

tively. This significant increase indicates crack coalescence and the formation of interconnected pore networks caused by severe thermal decomposition and structural disintegration.

From an overall trend perspective, as the temperature rises, the specific surface area of 3DPC generally decreases, especially at 400 °C and 600 °C, when the pore structure tends to be dense and micro-cracks and pores gradually increase. However, at 800 °C, the specific surface area and pore volume showed a significant recovery. This change can be attributed to the pyrolysis reaction at high temperatures and the formation of new phases, which led to a sharp increase in porosity and surface area. This phenomenon indicates that under high-temperature fire or other high-temperature treatment conditions, the microstructure and mechanical properties of 3DPC may be severely affected, especially above 800 °C, where the embrittlement of the structure and the increase of pores may lead to serious degradation of the material. The sharp increase in pore volume at 800 °C marks a transition from a densification-controlled regime to a damage-dominated regime, which fundamentally explains the drastic deterioration of mechanical properties at ultra-high temperatures.

3.6. SEM analysis

At room temperature (RT), the 3DPC specimen exhibits a dense, well-hydrated microstructure (Fig. 10(c)), contributing to its high initial compressive strength. The matrix consists mainly of amorphous C-S-H gel, binding unhydrated cement particles and fine aggregates (Fig. 10(b)). Abundant crystalline hydration products are present, including fine needle-like ettringite (AFt) crystals forming an interwoven network, as well as distinct hexagonal portlandite ($Ca(OH)_2$) crystals (Fig. 10(a)). The basalt fibers are well-embedded in the matrix without significant interfacial transition zone (ITZ) defects (Fig. 10(c)). This dense C-S-H gel, crystalline phases, and strong fiber–matrix bonding collectively enhance the material's mechanical properties before thermal exposure.

At 200 °C, the microstructure of 3DPC begins to deteriorate through initial decomposition of hydration products and formation of functional pore structures. Although no macroscale thermal cracks are visible, the overall structure becomes noticeably looser. The C–S–H gel undergoes dehydration shrinkage and agglomeration, reducing its specific surface area and forming micropores (Fig. 11b), thereby weakening cementitious bonding [39]. Simultaneously, acicular ettringite (AFt) crystals lose integrity, showing blunted tips and edge erosion (Fig. 11(a)), indicating conversion to amorphous phases and loss of micro-anchoring capacity [30]. A key microstructural change is the formation of continuous microchannels due to melted polypropylene (PP) fibers (Fig. 11(c)), which serve as pressure-relief pathways by releasing vapour from capillary and bound water during heating, mitigating internal pressure [40]. The performance degradation at this temperature results from combined chemical-physical mechanisms, with no significant thermomechanical microcracking observed. This damage preconditions the material for crack initiation and propagation at higher temperatures.

At 400 °C, the microstructure of 3DPC reaches a critical transformation point, driven by synergistic chemical decomposition and physical damage mechanisms that are severely exacerbated by subsequent water cooling. Chemically, key hydration products decompose extensively: well-defined $Ca(OH)_2$ crystals break down, and the dense C–S–H gel network disintegrates irreversibly, transforming into a porous, fragile honeycomb-like skeleton (Fig. 12(a)(b)). This degradation causes a substantial loss of cementation and mechanical strength. Physically, heating-induced microcracking from dehydration shrinkage and portlandite decomposition is dramatically amplified during rapid water cooling.

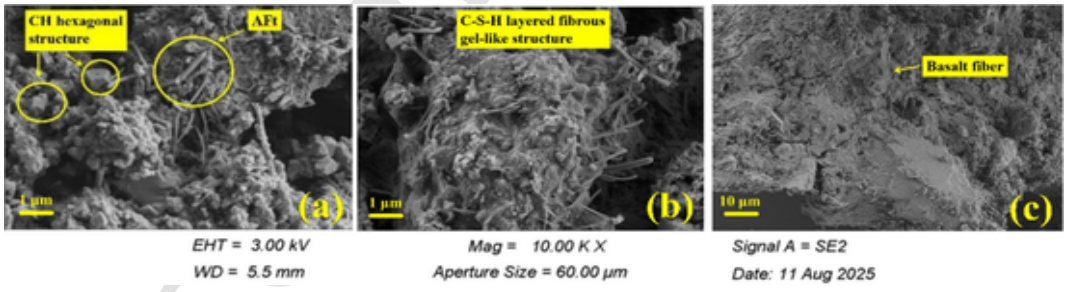

Fig. 10. SEM micrographs of the 3DPC specimen at room temperature (RT).

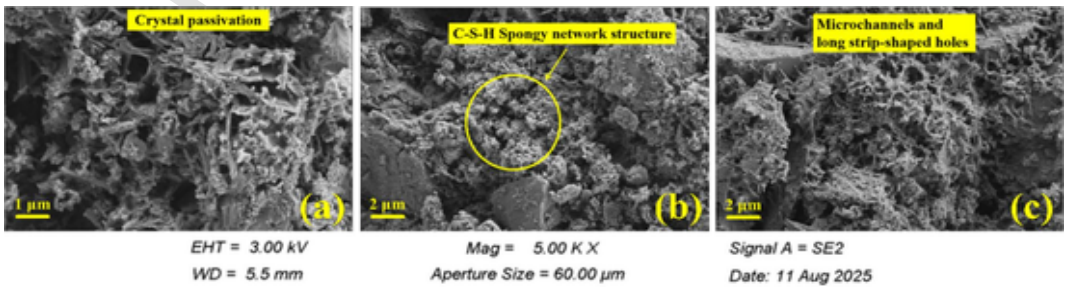

Fig. 11. SEM micrographs of the 3DPC specimen after exposure to 200 °C and water cooling.

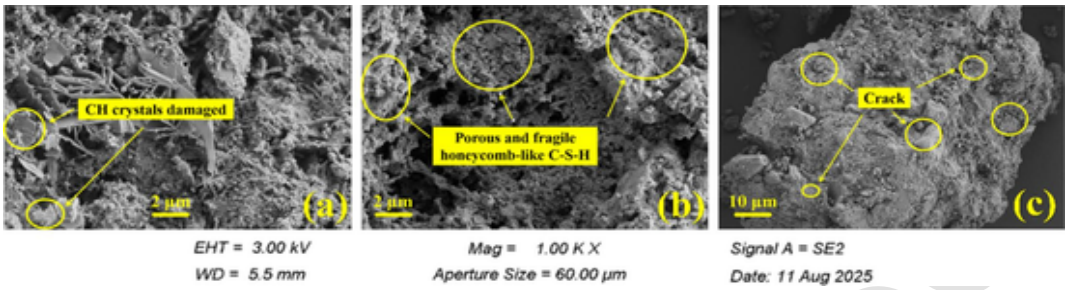

Fig. 12. SEM micrographs of the 3DPC specimen after exposure to 400 °C and water cooling.

The severe thermal gradient generates intense tensile stresses, acting on the already weakened matrix and causing microcracks to expand, interconnect, and propagate into a large-scale crack network (Fig. 12(c)), resulting in comprehensive structural failure.

At 600 °C, the microstructure of 3DPC undergoes complete and irreversible collapse, with damage extending beyond hydration product decomposition. The cementitious matrix fully loses its cohesion, leaving a highly porous and fragile calcium-silicate oxide skeleton with no binding capacity Fig. 13(a). A critical damage mechanism is triggered by the α–β phase transition of quartz aggregates near 573 °C, which involves sudden volumetric expansion [41]. This generates intense internal wedging stresses within the already brittle matrix, leading to extensive cracking and disintegration. Pronounced gaps and fracture zones between aggregates and the matrix are visible in Fig. 13(b). Subsequent rapid water cooling propagates this damage throughout the material via severe thermal shock. The melting point of PP fibers is typically in the range of 160–170 °C; Under exposure to 600 °C, they undergo completely melting followed by thermal degradation. Consequently, intact fibrous morphologies are no longer observable in SEM images. In contrast, basalt fiber exhibits superior thermal stability and can retain a relatively intact fiber morphology at 600 °C, allowing clearly distinguishable and continuous solid fiber structures to be identified in the micrographs, as shown in Fig. 13(c), the surface of basalt fibers exhibited visible longitudinal microcracks, accompanied by localized surface degradation and brittle fracture. Meanwhile, the interfacial bonding between the fiber and the surrounding mortar matrix was substantially deteriorated. As a result, the fibers acted merely as stress-inactive inert fillers within the fragmented matrix, thereby losing their reinforcing effectiveness.

At the extreme temperature of 800 °C, the microstructure of 3DPC underwent a catastrophic disintegration in its final stage. Its unique damage mechanism is the result of the combined effect of high-temperature chemical decomposition and destructive rehydration reactions induced by water cooling. It can be clearly seen from Fig. 14(a) that the material has been completely pulverized. The interface between the original matrix, aggregates and fibers no longer exists, replaced by an extremely loose and disordered accumulation composed of tiny particles and fragments. This form directly explains the phenomenon that it almost completely loses its strength on a macroscopic level. The decisive damage mechanism at this stage is triggered at the moment of rapid water cooling (quenching). During the holding process at 800 °C, not only have the hydration products completely decomposed, but the calcium carbonate ($CaCO_3$) formed due to carbonization in the matrix has also begun to decompose, generating a large amount of

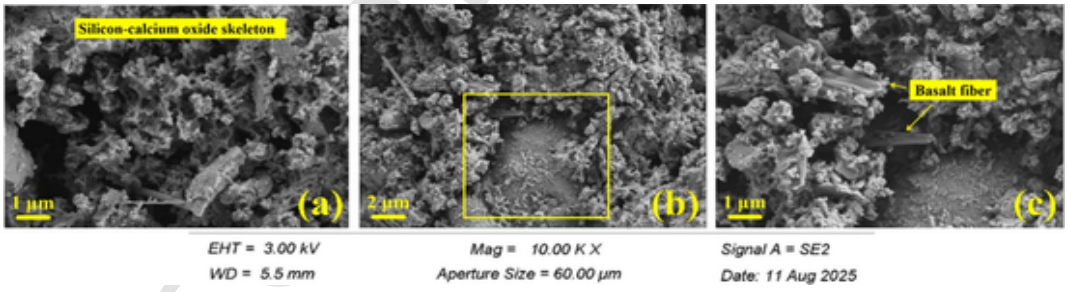

Fig. 13. SEM micrographs of the 3DPC specimen after exposure to 600 °C and water cooling.

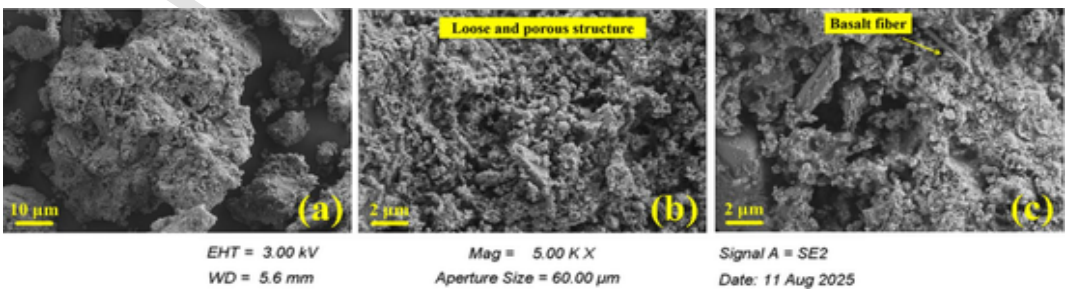

Fig. 14. SEM micrographs of the 3DPC specimen after exposure to 800 °C and water cooling.

highly active new calcium oxide (CaO). When this hot, porous sample was thrown into cold water, water quickly seeped into its interior. This triggered a vigorous rehydration reaction of CaO (the digestion reaction of slaked lime: $CaO + H_2O \rightarrow Ca(OH)_2$). This reaction has two fatal characteristics: ① Intense volume expansion: The volume of newly generated $Ca(OH)_2$ is much larger than that of the reactant CaO, which generates a huge crystallization pressure at the microscopic scale. ② Instantaneous occurrence: The reaction speed is extremely fast, and the resulting expansion stress is applied instantaneously. This internal, instantaneous and huge expansion stress completely shatters the residual skeleton that has become brittle and porous at 600 °C. This "rehydration and powderization" effect is the core reason for the unique deterioration phenomenon of water-cooled samples at 800 °C. Its direct manifestation in microscopic morphology is the loose and porous structure observed in Fig. 14(b). This structure is a typical feature of the material after it is cracked and crushed from the inside, and it also explains why the specific surface area of the 800 °C sample experiences explosive growth in BET analysis. Under such extreme damage, the condition of basalt fibers becomes even worse than at 600 °C. As shown in Fig. 14 (c), the fibers are completely "stripped" from the matrix, with only some powdered matrix debris loosely adhering to their surfaces. They are no longer the reinforcements in the composite material, but merely inert impurities scattered in the powder-like debris, and their reinforcing and bridging effects have completely vanished.

As shown in Fig. 15(a), the fibers at ambient temperature maintain an intact morphology, and the fracture surface exhibits a characteristic fibrillated appearance indicative of ductile tensile failure, consistent with the typical behavior of PP fibers under normal conditions. The opposite end of the fiber remains firmly embedded in the cementitious matrix, demonstrating strong interfacial bonding, which contributes to enhanced mechanical strength and improved ductility of the specimen. Given that PP fibers begin to melt at approximately 160–170 °C, they would not preserve an intact fibrous morphology at 200 °C, as observed in Fig. 15(b). Therefore, the fiber shown in this image—characterized by higher thermal stability and a brittle fracture surface—can be identified as basalt fiber. Its tight bonding with the mortar matrix indicates its significant role in sustaining the mechanical performance of the specimen at elevated temperatures.

At 400 °C, the PP fibers have completely melted. As illustrated in Fig. 15(c), their melting leaves smooth-walled cylindrical channels within the mortar matrix, which function as effective pressure-relief pathways under high-temperature exposure. These channels alleviate internal vapor pressure buildup, thereby mitigating damage associated with outward expansive stresses. The surrounding mortar appears relatively intact, forming a pronounced contrast with the more severely deteriorated microstructure observed in Fig. 15(d) at the same temperature.

3.7. Degradation mechanism

The thermal degradation of 3DPC under high-temperature exposure followed by rapid water cooling involves complex multi-scale mechanisms, spanning from molecular-level bond disruption to macroscopic structural failure. Through the investigation of the evolution of chemical bonds, the transformation of microstructure and their synergistic effects on mechanical properties, this section expounds the basic mechanisms of the performance deterioration of 3DPC.

3.7.1. Interfacial degradation and 3DPC vulnerabilities

The anisotropic nature of 3DPC promotes degradation through interfacial bond failure [42]. Interlayer zones, characterized by lower hydration product density and higher fractions of unstable phases (e.g., et-

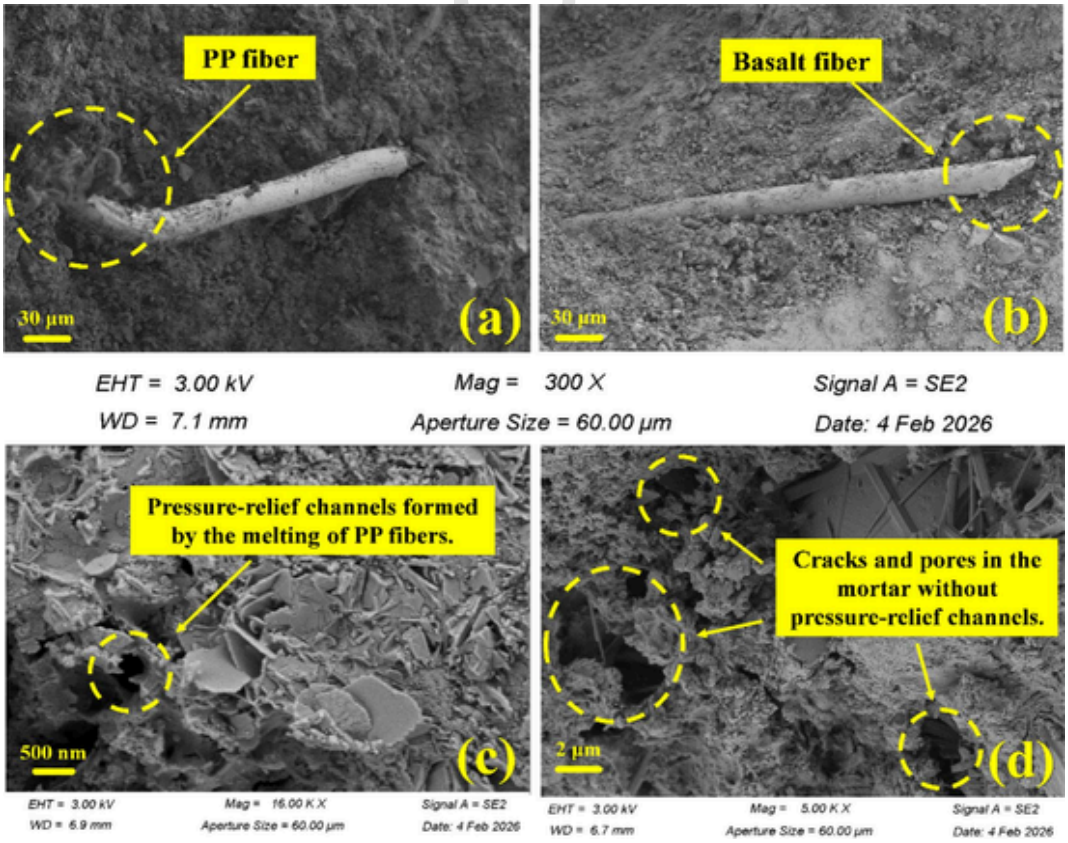

Fig. 15. SEM micrographs of the fibers in 3DPC specimen.

tringite and monosulfate), are prone to decomposition under heating [43]. A mismatch in the coefficient of thermal expansion (CTE) between the bulk material (~10–12 × 10^{-6}/°C) and the more porous interface further concentrates thermal stress, often exceeding the already weakened bond strength and initiating debonding [44]. Additionally, shear-induced alignment of C-S-H during printing raises CTE perpendicular to the deposition direction, amplifying interfacial stress and accelerating degradation [45].

3.7.2. Molecular-level degradation mechanisms

Thermal degradation progressively disrupts the chemical bonds in hydration products, fundamentally altering the cementitious matrix. The decomposition of calcium silicate hydrate (C-S-H) begins at low temperatures, involving depolymerization and reorganization of silicate chains (SiO_4 tetrahedra linked by bridging oxygen) [46]. As shown in the mass-loss curve (Fig. 8(a)), an initial weight-loss stage occurs within 50–105 °C, which is attributed to the evaporation of physically adsorbed and interlayer water. This process involves the rupture of weak hydrogen bonds, generating capillary tension and microshrinkage within the matrix. Concurrently, the reduction in compressive strength observed at 200 °C (Fig. 6) indicates that moisture migration alone is sufficient to induce measurable structural deterioration. As temperature increases to approximately 200 °C and beyond, more substantial chemical changes occur. Chemically bound water is removed through the condensation of adjacent silanol (Si-OH) groups, following the reaction: 2Si-OH → Si-O-Si + H_2O. This dehydroxylation reaction forms new silicate linkages, which increases the degree of polymerization of the silicate network. Concurrently, the loss of water molecules causes the collapse of the nanoscale gel pores, significantly reducing the specific surface area of the C-S-H gel (from approximately 100–150 m^2/g to lower values) and increasing its coarseness. Infrared spectroscopy confirms this structural evolution. The characteristic Si-O stretching vibrations often shift to higher wavenumbers, indicating an increase in the degree of silicate polymerization and the formation of stronger, shorter Si-O-Si bonds [47]. Despite this local strengthening of the silicate network, the overall mechanical properties of the cement paste deteriorate severely. This is due to the collective effects of mass loss, increased porosity, and the breakdown of the original cohesive calcium-silicate hydrate framework. The binding mechanism, which originally relied on a continuous nanostructured hydrated phase, is compromised, and residual strength becomes increasingly dependent on the frictional forces and mechanical interlocking of the degraded, coarse particles [48]. The layered structure of Portland stone ($Ca(OH)_2$) contains a relatively weak hydrogen bond network, which makes its thermal stability poor. When heated to 400-500 °C, thermal energy breaks these hydrogen bonds and triggers a dehydroxylation reaction: protons (H^+) from adjacent hydroxyl ions (OH^-) and hydroxide ions (OH^-) combine through an endothermic reaction to form water molecules ($Ca(OH)_2 \rightarrow CaO + H_2O$). This process generates CaO with high specific surface area and activity. The calcium ion and oxygen ion sites on its surface can serve as nucleation sites, driving the subsequent rehydration reaction with water molecules. During the rapid water-cooling stage, CaO rapidly rehydrates to form $Ca(OH)_2$, accompanied by significant volumetric expansion. This volume increase readily induces microcrack development within the matrix. Subsequently, during storage or exposure to atmospheric conditions, the rehydrated $Ca(OH)_2$ further reacts with CO_2 to form $CaCO_3$.

Compared with the $CaCO_3$ formed during the original hydration or natural carbonation processes, the carbonate regenerated after high-temperature exposure precipitates rapidly and is typically characterized by a relatively loose and disordered microstructure. As a result, it is unable to reconstruct a continuous and dense binding framework. Consequently, its contribution to strength recovery is limited, and the overall structure continues to exhibit pronounced deterioration, as reflected by the significant strength reduction observed between 600 °C and 800 °C in Fig. 6.

3.7.3. Thermal shock-induced macroscopic void formation and microcracking

The rapid cooling of the surface in contact with water following exposure to elevated temperatures introduces severe thermal gradients, generating catastrophic macroscopic cracking [49,50]. This thermal shock mechanism is initiated by differential thermal contraction, wherein the surface layers undergo rapid cooling and contraction while the interior remains hot and expanded. This results in substantial tensile stresses that surpass the tensile strength of the thermally weakened matrix. The damage severity is closely related to the pre-existing microstructural condition of the material. During the prior heating phase, the melting of PP fibers (at ~ 165 °C) forms a network of microchannels [50]. As shown in Fig. 15(c), these channels function as pressure-relief pathways during heating to mitigate the risk of explosive spalling; however, they simultaneously create localized low-density regions that act as potential damage initiation sites during the subsequent thermal shock stage. Furthermore, the coupled effects of high temperature and thermal shock lead to significant damage in 3DPC due to its inherent weaknesses at interlayer interfaces. The combination of reduced bond strength and anisotropic thermal expansion creates preferential paths for crack propagation along the printed layers. High-resolution SEM analysis reveals complex branching crack patterns that often align with the printing direction [51]. It is critical to distinguish this thermal-shock-driven damage from the damage that occurs during the heating phase. During heating, the release of physically and chemically bound water can generate internal vapor pressures reaching 5–15 MPa, particularly above 300 °C [23]. If this pressure is not effectively relieved through the channels formed by the melting of PP fibers, it leads to the development of internal microcracks and spherical voids. As the heating stage progresses, the accumulation of micro-damage further weakens the matrix, facilitating crack propagation and coalescence within the already deteriorated structure. Consequently, the mortar becomes increasingly porous and loose, forming extensive voids and interconnected cracks, as illustrated in Fig. 15(d).

3.7.4. Fiber reinforcement failure mechanisms

The degradation of fiber reinforcement in 3DPC under thermal shock conditions follows a complex progression involving both fiber–matrix interfacial failure and intrinsic fiber property changes. Although basalt fibers are more thermally stable than polymer fibers, they undergo significant strength degradation above approximately 600 °C [52], while also experiencing progressive bond deterioration with the surrounding matrix as hydration products decompose. The interfacial transition zone (ITZ) surrounding basalt fibers experiences preferential degradation due to its inherent higher porosity and distinct chemical composition compared to the bulk matrix [53]. At temperatures ranging from 200 to 400 degrees Celsius, the decomposition of C-S-H gel within the ITZ leads to a reduction in the chemical adhesion between fibers and the matrix. This transition results in a shift from a chemical bonding-based load transfer mechanism to one that is primarily frictional in nature. This degradation is exacerbated by the differential thermal expansion between basalt fibers and the concrete matrix, leading to progressive debonding [54]. During the thermal shock stage, the matrix undergoes rapid dimensional changes, subjecting the fibers to additional mechanical pulling and shearing forces, which further causes the damage. As shown in Figs. 13(c) and 14(c), after heat treatment at 600 °C and 800 °C, the basalt fibers exhibit evident surface deterioration, while the cementitious matrix simultaneously undergoes extensive decomposition. Under these conditions, this dual degradation of both the fibers and the surrounding matrix renders the fibers nearly incapable of providing effective structural reinforcement. The PP fibers exhibit a dual role that undergoes a transformation in response to varia-

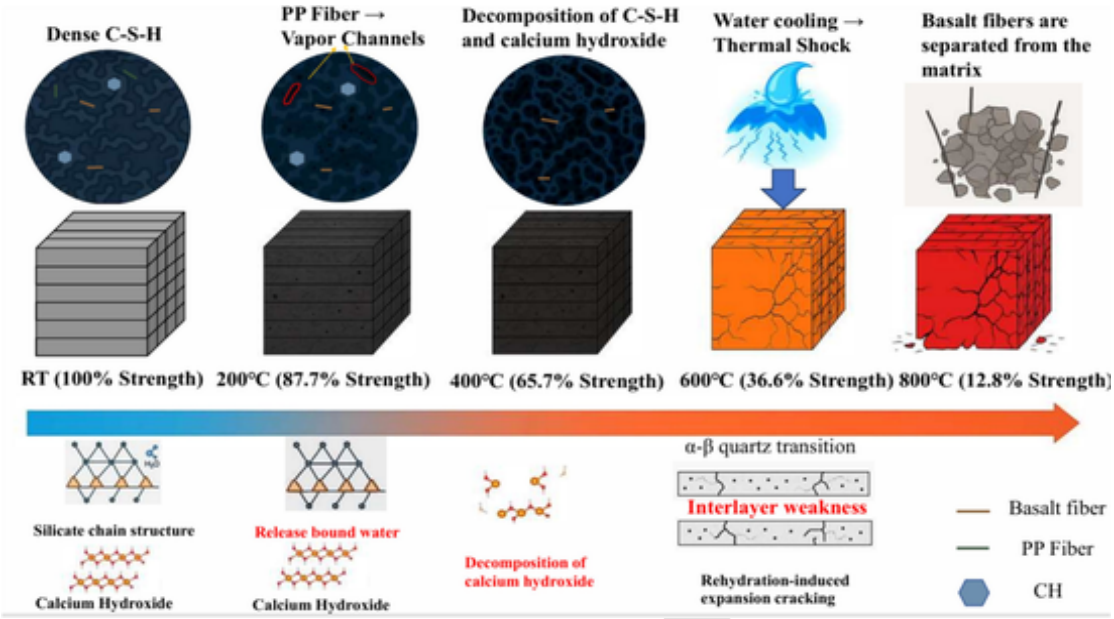

Fig. 16. Multiscale Schematic of the Degradation Mechanisms in 3DPC Subjected to High Temperature and Rapid Water Cooling.

tions in temperature. At ambient temperatures, they provide valuable reinforcement by improving ductility, controlling crack propagation, and enhancing toughness [55]. Their melting (~165 °C) creates channels that provide beneficial pressure relief, thereby preventing explosive spalling during the initial heating process. Subsequent thermal shock results in the filling of these channels with water, which facilitates crack propagation during the cooling phase due to hydraulic pressure and capillary action. These water-filled channels also create additional sites for potential future freeze–thaw damage if the material is exposed to sub-zero temperatures Fig. 16.

3.7.5. Synergistic degradation and failure progression

The overall degradation of 3DPC under thermal shock represents a synergistic combination of all previously described mechanisms, with each damage mode interacting with others. The sequence of events is characterized by a set of hallmark stages, namely: initial molecular bond weakening, interfacial debonding, macroscopic void formation, thermal shock cracking, rehydration-induced expansion cracking [56], and complete structural failure. The critical temperature threshold for catastrophic failure is situated between 400 and 600 °C, where multiple degradation mechanisms reach their peak intensity concurrently. Within this temperature range, the decomposition of primary hydration products, the α-β quartz transition in aggregates (at ~ 573 °C) [57], although the α–β quartz transition at approximately 573 °C is a reversible displacive transformation involving tetrahedral rotation without bond breakage, the associated abrupt volumetric expansion induces transient internal stresses within the cementitious matrix. Due to thermal incompatibility between quartz aggregates and the surrounding paste, stress concentration develops at the interfacial transition zone (ITZ), leading to irreversible microcrack formation. Upon cooling, the crystal symmetry of quartz is restored; Upon cooling, the crystal symmetry of quartz is restored; however, the thermally induced microstructural damage remains, resulting in permanent mechanical degradation despite the apparent phase reversibility in XRD analysis. And maximum thermal shock sensitivity [58] synergistically generate structural degradation. The water-cooling phase is a critical component of the coupled deterioration process, where various damage mechanisms occur through rapid thermal gradients, chemical rehydration, and potential phase change effects. The cooling rate exerts a substantial influence on the extent of damage, with accelerated cooling rates (>50 °C/min) resulting in more pronounced microcracking but potentially mitigated chemical rehydration damage due to diminished reaction time. The inherent interlayer weakness of 3DPC renders it particularly vulnerable to this multi-mechanism degradation, with failure preferentially occurring along printing interfaces where all damage modes are amplified by the pre-existing structural discontinuities and reduced hydration product density.

4. Conclusions

This study investigates the degradation of 3DPC under thermal shock (up to 800 °C with rapid water cooling, simulating firefighting). Combined mechanical and multi-scale microstructural analyses (SEM, XRD, TGA, BET) reveal a synergistic degradation mechanism that is markedly more severe than from isothermal heating alone.

The combined conditions of elevated temperatures and rapid water quenching induce severe thermal gradients, leading to catastrophic macroscopic cracking and comprehensive microstructural disintegration. Under this severe coupled scenario, the residual compressive strength of 3DPC decreased sharply with temperature, suffering a near-total loss (87.2% reduction) at 800 °C

A synergistic degradation mechanism occurs between 400 and 600 °C, where the dehydroxylation of portlandite, decomposition of C-S-H gel, and the α-β quartz phase transition (~573 °C) in aggregates coincide. This leads to microstructural collapse and a sharp decline in mechanical properties

The degradation progresses through distinct temperature stages: <200 °C: Evaporation of free water and partial C-S-H dehydration, PP fibers melt to form mechanically weak but stress-relieving channels. 200–400 °C: The bound water in the gel material is removed. 400–600 °C: Synergistic degradation occurs due to portlandite dehydroxylation, C-S-H decomposition, and quartz α-β transition (~573 °C), causing volumetric expansion and extensive microcracking. > 600 °C: The cement matrix fully decomposes. At 800 °C, water quenching triggers rapid rehydration of highly reactive CaO, generating expansive stresses that disintegrate the material into a friable granular state

Both PP and basalt fibers play dual, temperature-dependent roles. PP fibers enhance ductility at ambient temperature and form pressure-relief channels upon melting, which help alleviate internal vapor pressure at elevated temperatures. Basalt fibers provide stable reinforcement at moderate temperatures; however, their effectiveness diminishes above 600 °C due to microcracking and interfacial degradation. Overall, the high-temperature performance of the mortar is governed by the synergistic yet temperature-sensitive behavior of the two fibers

BET analysis revealed a non-linear evolution of porosity. The specific surface area initially decreased up to 600 °C due to pore coarsening and collapse but then increased substantially at 800 °C as a result of extensive microcracking and material pulverization caused by thermal shock and rehydration expansion

This work highlights the extreme vulnerability of 3DPC to combined high-temperature and rapid water cooling—a previously overlooked yet critical scenario. The results demonstrate that post-fire safety assessments after water suppression cannot be extrapolated from slow-cooling or isothermal data. These findings provide essential insights for realistic safety evaluation and form a basis for developing more resilient 3DPC mixtures and targeted fire protection strategies in digital construction. Future research should focus on mitigating interlayer weakness and improving thermal shock resistance through approaches such as optimizing fiber blends, incorporating nano-reinforcements, or designing protective coatings.

CRediT authorship contribution statement

Hongru Zhou: Writing – review & editing, Methodology, Investigation. **Linsen Zhang:** Writing – review & editing, Conceptualization. **Hideki Yoshioka:** Supervision, Project administration, Funding acquisition. **Muying Ge:** Writing – review & editing, Data curation. **Kai Wang:** Writing – review & editing, Formal analysis. **Bochao Sun:** Supervision, Resources. **Ziyi Lu:** Formal analysis, Data curation. **Biao Zhou:** Writing – original draft, Validation, Conceptualization.

Declaration of competing interest

The authors declare that they have no known competing financial interests or personal relationships that could have appeared to influence the work reported in this paper.

Acknowledgments

This work was supported by he Ordos Key Research and Development Program (No.YF20240026) , National Natural Science Foundation of China (No.52374248), Beijing Nova Program (No. 202504841008) and the Fundamental Research Funds for the Central Universities (No. 2025ZKPYAQ03).

Data availability

Data will be made available on request.

References

[1] A.R. Arunothayan, A. Ramesh, J.G. Sanjayan, Fire resistance of 3D printed ultra-high performance concrete panels, J. Build. Eng. 98 (2024) 111100, https://doi.org/10.1016/j.jobe.2024.111100.
[2] O. Arioz, Effects of elevated temperatures on properties of concrete, Fire Saf. J. 42 (8) (2007) 516–522, https://doi.org/10.1016/j.firesaf.2007.01.003.
[3] B. Fernandes, et al., Microstructure of concrete subjected to elevated temperatures: physico-chemical changes and analysis techniques, Revista IBRACON de Estruturas e Materiais 10 (2017) 838–863, https://doi.org/10.1590/S1983-41952017000400004.
[4] G. Ahmed, A review of "3D concrete printing": materials and process characterization, economic considerations and environmental sustainability, J. Build. Eng. 66 (2023) 105863, https://doi.org/10.1016/j.jobe.2023.105863.
[5] B. Georgali, P.E. Tsakiridis, Microstructure of fire-damaged concrete. A case study, Cem. Concr. Compos. 27 (2) (2005) 255–259, https://doi.org/10.1016/j.cemconcomp.2004.02.022.
[6] M. Nodehi, et al., Durability properties of 3D printed concrete (3DPC), Automat. Constr. 142 (2022) 104479, https://doi.org/10.1016/j.autcon.2022.104479.
[7] I. Hager, A. Golonka, R. Putanowicz, 3D printing of buildings and building components as the future of sustainable construction? Proc. Eng. 151 (2016) 292–299, https://doi.org/10.1016/j.proeng.2016.07.357.
[8] M. Pasztetnik, R. Wróblewski, A literature review of concrete ability to sustain strength after fire exposure based on the heat accumulation factor, Materials (Basel) 14 (16) (2021), https://doi.org/10.3390/ma14164719.
[9] S. Fehérvári, Effect of cooling methods on the residual properties of concrete exposed to elevated temperature, Results Eng. 16 (2022) 100797, https://doi.org/10.1016/j.rineng.2022.100797.
[10] A. Alaskar, A comprehensive review on the influence of elevated temperatures on the mechanical performance of high-performance concretes, J. Umm Al-Qura Univers. Eng. Architect. (2025), https://doi.org/10.1007/s43995-025-00199-w.
[11] L. Segalin, et al., Effect of cooling method on concrete compressive strength after exposure to high temperatures, Semina 41 13 (2020), https://doi.org/10.5433/1679-0375.2020v41n1p13.
[12] A.J. Babafemi, et al., A concise review on interlayer bond strength in 3D concrete printing, Sustainability 13 (13) (2021) 7137, https://doi.org/10.3390/su13137137.
[13] A. Cicione, et al., An experimental study of the behavior of 3D printed concrete at elevated temperatures, Fire Saf. J. 120 (2021) 103075, https://doi.org/10.1016/j.firesaf.2020.103075.
[14] Lee, Y.J., et al., Interlayer Bond Strength of 3D Printed Concrete Members with Ultra High Performance Concrete (UHPC) Mix. Buildings, (2024) 14(7) 2060.https://doi.org/10.3390/buildings14072060
[15] W. Botte, R. Caspeele, Post-cooling properties of concrete exposed to fire, Fire Saf. J. 92 (2017) 142–150, https://doi.org/10.1016/j.firesaf.2017.06.010.
[16] Napolitano, R., et al. Dynamic Behaviour of Layered 3D Printed Concrete Elements. in Second RILEM International Conference on Concrete and Digital Fabrication. 2020. Cham: Springer International Publishing. https://doi.org/10.1007/978-3-030-49916-7_49.
[17] J. Xiao, et al., Mechanical and microstructural evolution of 3D printed concrete with polyethylene fiber and recycled sand at elevated temperatures, Constr. Build. Mater. 293 (2021) 123524, https://doi.org/10.1016/j.conbuildmat.2021.123524.
[18] F. El Inaty, B. Baz, G. Aouad, Long-term durability assessment of 3D printed concrete, J. Adhes. Sci. Technol. 37 (12) (2022) 1921–1936, https://doi.org/10.1080/01694243.2022.2102717.
[19] L. Wang, et al., Mechanical and microstructural properties of 3D-printed aluminate cement based composite exposed to elevated temperatures, Constr. Build. Mater. 353 (2022) 129144, https://doi.org/10.1016/j.conbuildmat.2022.129144.
[20] O. Park, et al., Influence of elevated temperature on the microstructures and mechanical properties of cement-based mortar with sands and refractory materials, J. Korean Ceram. Soc. 61 (6) (2024) 1050–1057, https://doi.org/10.1007/s43207-024-00415-8.
[21] S. Han, et al., Graphene-oxide-reinforced cement composites mechanical and microstructural characteristics at elevated temperatures, Nanotechnol. Rev. 11 (1) (2022) 3174–3194, https://doi.org/10.1515/ntrev-2022-0495.
[22] Z. Yu, et al., Study on the fracture mechanical properties of high performance concrete (HPC) with rapid cooling after high temperature, Constr. Build. Mater. 422 (2024) 135718, https://doi.org/10.1016/j.conbuildmat.2024.135718.
[23] U. Pulkit, S.D. Adhikary, Effect of micro-structural changes on concrete properties at elevated temperature: current knowledge and outlook, Struct. Concr. 23 (4) (2021) 1995–2014, https://doi.org/10.1002/suco.202000365.
[24] Y.-F. Fu, et al., Experimental study of micro/macro crack development and stress–strain relations of cement-based composite materials at elevated temperatures, Cem. Concr. Res. 34 (5) (2004) 789–797, https://doi.org/10.1016/j.cemconres.2003.08.029.
[25] H. Jiang, et al., Mechanical and microstructural performance of UHPC with recycled aggregates modified by basalt fiber and nanoalumina at high temperatures, Materials 18 (5) (2025) 1072, https://doi.org/10.3390/ma18051072.
[26] Y. Che, H. Yang, Hydration products, pore structure, and compressive strength of extrusion-based 3D printed cement pastes containing nano calcium carbonate, Case Stud. Constr. Mater. 17 (2022) e01590, https://doi.org/10.1016/j.cscm.2022.e01590.
[27] H.E.D.H. Seleem, A.M. Rashad, T. Elsokary, Effect of elevated temperature on physico-mechanical properties of blended cement concrete, Constr. Build. Mater. 25 (2) (2011) 1009–1017, https://doi.org/10.1016/j.conbuildmat.2010.06.078.
[28] G.-F. Peng, Z.-S. Huang, Change in microstructure of hardened cement paste subjected to elevated temperatures, Constr. Build. Mater. 22 (4) (2008) 593–599, https://doi.org/10.1016/j.conbuildmat.2006.11.002.
[29] E. Tajuelo Rodriguez, et al., Thermal stability of C-S-H phases and applicability of Richardson and Groves' and Richardson C-(A)-S-H(I) models to synthetic C-S-H, Cem. Concr. Res. 93 (2017) 45–56, https://doi.org/10.1016/j.cemconres.2016.12.005.
[30] Q. Zhang, G. Ye, Dehydration kinetics of Portland cement paste at high temperature, J. Therm. Anal. Calorim. 110 (1) (2012) 153–158, https://doi.org/10.1007/s10973-012-2303-9.
[31] N. Vogler, et al., Description of the concrete carbonation process with adjusted depth-resolved thermogravimetric analysis, J. Therm. Anal. Calorim. 147 (11)

(2022) 6167–6180, https://doi.org/10.1007/s10973-021-10966-1.
[32] A. Gholizadeh-Vayghan, et al., Thermal reactivation of hydrated cement paste: properties and impact on cement hydration, Materials (Basel) 17 (11) (2024), https://doi.org/10.3390/ma17112659.
[33] L. Soriano, et al., Use of high-resolution thermogravimetric analysis (HRTG) technique in spent FCC catalyst/Portland cement pastes, J. Therm. Anal. Calorim. 120 (3) (2015) 1511–1517, https://doi.org/10.1007/s10973-015-4526-z.
[34] S. Xue, et al., Influence of water re-curing on microstructure of heat-damaged cement mortar characterized by low-field NMR and MIP, Constr. Build. Mater. 262 (2020) 120532, https://doi.org/10.1016/j.conbuildmat.2020.120532.
[35] K.S. Walton, R.Q. Snurr, Applicability of the BET method for determining surface areas of microporous metal–organic frameworks, J. Am. Chem. Soc. 129 (27) (2007) 8552–8556, https://doi.org/10.1021/ja071174k.
[36] T.S. van Erp, J.A. Martens, A standardization for BET fitting of adsorption isotherms, Microporous Mesoporous Mater. 145 (2011) 188–193, https://doi.org/10.1016/j.micromeso.2011.05.022.
[37] Long Khánh Nguyễn, u., Ứng dụng phương pháp thí nghiệm BET, BJH và DFT xác định diện tích bề mặt riêng và phân bố kích thước lỗ rỗng của vật liệu bê tông. Tạp chí điện tử Khoa học và Công nghệ Giao thông, (2024) 40-50. Doi: 10.58845/jstt.utt.2024.vn.4.2.40-50.
[38] B. Zhou, et al., Mechanical and microstructure evolution of 3D printed concrete interlayer at elevated temperatures, J. Build. Eng. 107 (2025) 112706, https://doi.org/10.1016/j.jobe.2025.112706.
[39] E. John, B. Lothenbach, Cement hydration mechanisms through time – a review, J. Mater. Sci. 58 (24) (2023) 9805–9833, https://doi.org/10.1007/s10853-023-08651-9.
[40] H.G. Şahin, et al., Degradation of mechanical properties of 3D fiber reinforced printed concrete mixtures exposed to elevated temperatures, Case Stud. Constr. Mater. (2025) 22, https://doi.org/10.1016/j.cscm.2025.e04506.
[41] B. Lawn, et al., Precipitous weakening of quartz at the α–β phase inversion, J. Am. Ceram. Soc. 104 (1) (2020) 23–26, https://doi.org/10.1111/jace.17470.
[42] L. Dong, et al., Chloride transport anisotropy and interfacial degradation in 3D-printed ultra-high-performance concrete: multi-scale evaluation and engineering implications, Constr. Build. Mater. 491 (2025) 142722, https://doi.org/10.1016/j.conbuildmat.2025.142722.
[43] D.W. Gardner, et al., Silicate bond characteristics in calcium–silicate–hydrates determined by high pressure raman spectroscopy, J. Phys. Chem. C 124 (33) (2020) 18335–18345, https://doi.org/10.1021/acs.jpcc.0c04563.
[44] N.A.M. Radzuan, et al., Layup sequence and interfacial bonding of additively manufactured polymeric composite: a brief review, Nanotechnol. Rev. 10 (1) (2021) 1853–1872, https://doi.org/10.1515/ntrev-2021-0116.
[45] J. Ma, et al., Effect of clay brick powder and recycled fine aggregates on properties of 3D printed concrete after high temperature exposure, Constr. Build. Mater. 491 (2025) 142676, https://doi.org/10.1016/j.conbuildmat.2025.142676.
[46] I.G. Richardson, The calcium silicate hydrates, Cem. Concr. Res. 38 (2) (2008) 137–158, https://doi.org/10.1016/j.cemconres.2007.11.005.
[47] Iftiquar, S., Structural Studies on Semiconducting Hydrogenated Amorphous Silicon Oxide Films. High Temperature Material Processes (An International Quarterly of High-Technology Plasma Processes), (2003) 6. Doi: 10.1615/HighTempMatProc.v6.i1.40.
[48] A. Madadi, J. Wei, Characterization of calcium silicate hydrate gels with different calcium to silica ratios and polymer modifications, Gels 8 (2) (2022), https://doi.org/10.3390/gels8020075.
[49] Wu, J., et al., An Experimental Study on the Influence of Different Cooling Methods on the Mechanical Properties of PVA Fiber-Reinforced High-Strength Concrete after High-Temperature Action. Polymers, (2024) 16(14) 2012. https://doi.org/10.3390/polym16142012.
[50] F. He, et al., A review on the mechanical characteristics of thermally damaged steel and polypropylene hybrid fiber-reinforced concretes, Arch. Civ. Mech. Eng. 24 (2) (2024) 69, https://doi.org/10.1007/s43452-024-00880-2.
[51] T. Ding, et al., Anisotropic behavior in bending of 3D printed concrete reinforced with fibers, Composite Structures 254 (2020) 112808, https://doi.org/10.1016/j.compstruct.2020.112808.
[52] J. Sim, C. Park, D.Y. Moon, Characteristics of basalt fiber as a strengthening material for concrete structures, Compos. Part B: Eng. 36 (6) (2005) 504–512, https://doi.org/10.1016/j.compositesb.2005.02.002.
[53] R.J.M. Wolfs, F.P. Bos, T.A.M. Salet, Hardened properties of 3D printed concrete: the influence of process parameters on interlayer adhesion, Cem. Concr. Res. 119 (2019) 132–140, https://doi.org/10.1016/j.cemconres.2019.02.017.
[54] A.M. Brandt, Fibre reinforced cement-based (FRC) composites after over 40 years of development in building and civil engineering, Composite Structures 86 (1) (2008) 3–9, https://doi.org/10.1016/j.compstruct.2008.03.006.
[55] P.S. Song, S. Hwang, B.C. Sheu, Strength properties of nylon- and polypropylene-fiber-reinforced concretes, Cem. Concr. Res. 35 (8) (2005) 1546–1550, https://doi.org/10.1016/j.cemconres.2004.06.033.
[56] I. Hager, Behaviour of cement concrete at high temperature, Bull. Polish Acad. Sci. Tech. Sci. (2013) 61, https://doi.org/10.2478/bpasts-2013-0013.
[57] U. Schneider, Concrete at high temperatures — A general review, Fire Saf. J. 13 (1) (1988) 55–68, https://doi.org/10.1016/0379-7112(88)90033-1.
[58] L. Li, M. Aubertin, A general relationship between porosity and uniaxial strength of engineering materials, Can. J. Civ. Eng. 30 (4) (2003) 644–658, https://doi.org/10.1139/l03-012.